

Half-Height Pin Gap Waveguide based Slow Wave Structure for Millimeter Wave Traveling-Wave Tubes

Amira Zied Abozied, Jonathan Gates, and Rosa Letizia, *Senior member, IEEE*

Abstract—The design of a W-band traveling-wave tube (TWT) power amplifier based on a groove gap waveguide slow wave circuit is presented in this paper. The technology of gap waveguide is analyzed to aid the design of electromagnetic band gap based slow wave structures in the upper millimeter wave range of the spectrum while alleviating some of the typical fabrication challenges at these frequencies. The results of Particle-In-Cell (PIC) simulations numerically demonstrate a 10-GHz instantaneous 3-dB bandwidth in the range 89-99 GHz with a minimum power gain of 25 dB. A prototype of the complete slow wave structure is manufactured via computer numerical control (CNC) machining and measured to verify the cold simulation results. Machining tolerances and surface roughness are also investigated. The design approach via groove gap waveguide is flexible and can be extended to alternative rectangular waveguide based slow wave structures.

Index Terms—Groove gap waveguide, half-height pin, traveling-wave tube, corrugated waveguide, millimeter waves.

I. INTRODUCTION

TRAVELING wave tube (TWT) amplifiers are capable of reaching unprecedented level of power compared to solid state amplifiers. This makes this technology especially attractive at the upper millimeter waves and THz frequency where they can unlock emerging applications in space and terrestrial high data rate wireless communications, imaging and plasma diagnostics. GaN solid state amplifiers at W-band have demonstrated 31 W output power in the 94-98 GHz range [1], whereas TWTs can reach and surpass 100 W in relatively broad bandwidths [2]–[4]. At this millimeter-size wavelength however, the small dimensions impose important constraints on the geometry of the TWT core component, the slow wave structure (SWS), and on the achievable surface quality, which make the classic helix TWT unsuitable above 70 GHz. Several alternative circuits have been proposed so far for the upper millimeter-waves and THz spectrum, including the folded waveguide, corrugated waveguide, gratings, ring bar and meander line configurations [2]. Among them, the corrugated waveguide combines ease of assembly to relatively good wave amplification when used with sheet electron beams. Several of these SWSs have been demonstrated via CNC micro-machining and LIGA (German acronym for Lithography, Electroplating and Molding) [5]–[7]. In this context, alternative waveguiding technology, based on the use of periodic arrangements, such as electromagnetic bandgap structures, have also been recently proposed to introduce single mode of operation in oversized structures and flexibility of design with functionalities integration [8]–[10]. For instance, in [8], a simple and scalable solution for wide, above the cutoff, beam tunnel designs was presented. The fundamental principle of these structures is to provide a region of frequencies where electromagnetic propagation is forbidden. These can then replace the metal walls of classical waveguides where waveguide confinement and propagation is achieved for 'modes' existing within

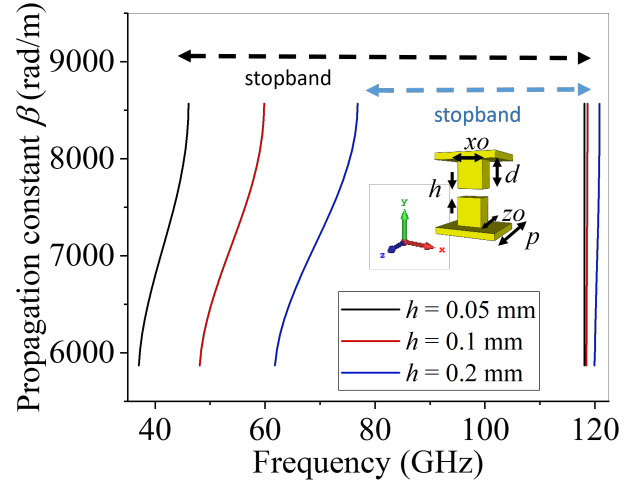


Fig. 1. Parametric study of the air gap h influence on the stopband characteristic of the half-height pin structure. The structure is periodic in the x - z plane, propagation along the z -direction is assumed. The unit cell is shown in inset where other parameters are chosen as $d = 0.61$ mm, $xo = 0.47$ mm, $zo = 0.58$ mm, $p = 1.1$ mm.

their stopband. This property can be exploited to suppress unwanted higher order modes in waveguides. The latter can be associated to critical oscillations for the operation of sheet beam TWTs, [11], [12]. At the millimeter wave frequencies, these concepts have found application as the so-called 'gap waveguide' which has emerged as a low-cost and low-loss solution. In fact, gap waveguides have the additional advantage to provide control of the RF signal without the need for electrical contact of the metal walls. Compared to other electromagnetic bandgap structures at these frequencies such as the one proposed in [8], the gap waveguide technology significantly alleviates the manufacturing challenges. This is obtained while retaining all the benefits of an all-metal rectangular waveguide as compared to the use of planar circuits [13]. Initial investigations of pin-based gap waveguide SWSs have been recently reported, [14]–[16]. In this paper, we propose the use of a novel groove gap waveguide configuration as the SWS waveguide enclosure. Synchronism with the electron beam is realized by means of a central corrugation. The stopband property of the gap waveguide is realized through the half-height pin structure, a configuration proposed for the first time in [17] and known for its broad bandwidth characteristics, [18]. A novel input/output 90-degree bend coupler based on the same topology is designed and experimentally demonstrated. Numerical simulations of the beam wave interaction predict a minimum of 25 dB gain in the 89-99 GHz range.

II. THE HALF-HEIGHT PIN GAP WAVEGUIDE-BASED SLOW WAVE STRUCTURE

The groove gap waveguide is used to replace the conventional enclosure of a rectangular waveguide-based SWS. The typical gap waveguide is made of two parallel plate surfaces, one perfect electric conductor (PEC), and one artificial magnetic conductor (AMC),

Amira Zied Abozied, Jonathan Gates and Rosa Letizia are with Lancaster University, School of Engineering, Lancaster, LA1 4YW, UK (email: a.ziedabozied@lancaster.ac.uk)

Rosa Letizia is also with the Cockcroft Institute, Warrington, U.K. (email: r.letizia@lancaster.ac.uk).

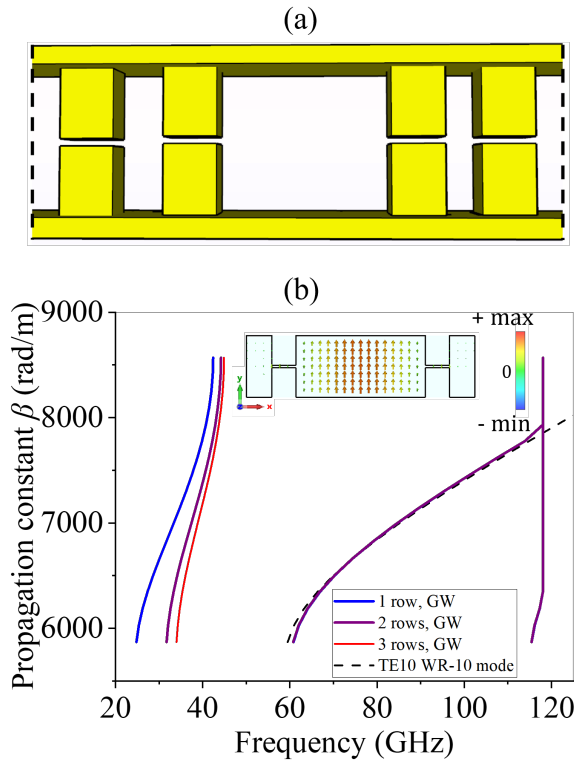


Fig. 2. Conceptual schematic of the W-band HHGW: the central groove has standard WR-10 dimensions (2.54 mm x 1.27 mm), the pins have dimensions as per Fig. 1 with $h = 0.05$ mm, (a); Band diagram comparison for the HHGW realized with 3, 2 and 1 row of pins on each side of the central groove and fundamental mode dispersion for the WR-10 waveguide. The E -field profile of the propagating mode for the 1-row HHGW is shown in inset, (b).

placed at a distance of less than $\lambda/4$. In this configuration, a frequency band-stop is generated where no electromagnetic propagation is permitted. When a metal guiding element is added, e.g. by adding a PEC longitudinal section within the AMC plate, a groove is created where certain modes, belonging to the stopband, can propagate. The AMC surface is in practice realized by a two-dimensional periodic structure. The most common gap waveguide (GW) employs the pin-structure as the AMC (also called 'bed of nails'). An example of the pin-based gap waveguide for SWS design (referred as the "full pin" GW-SWS in this work) is detailed in [14]. Here, an alternative configuration of the GW is considered, the half-height pin-based GW-SWS (HHGW-SWS). Compared to the full pin structure, the HHGW has been shown to provide wider stopband with lower aspect-ratio/lower height pins which facilitates their fabrication. The analytical model of the HHGW and a design example are reported in [18].

A. The HHGW-SWS unit cell

The geometry of the unit cell of the HHGW electromagnetic bandgap structure is shown in the inset of Fig. 1. Initial dimensions for the GW pin are set to have air gap of less than a quarter wavelength ($h < \lambda/4$), and the height of the pins defined by ($d + h = \lambda/2$) [13]. A numerical study of the dispersion of this periodic structure assuming the propagation direction in z was performed with the eigenmode solver of CST Studio Suite [19] (Fig. 1). From this Figure, it can be seen that a stopband around the frequency range of interest is realized for $d = 0.61$ mm, $x_o = 0.47$ mm, $z_o = 0.58$ mm and period p of 1.1 mm and that the air gap has

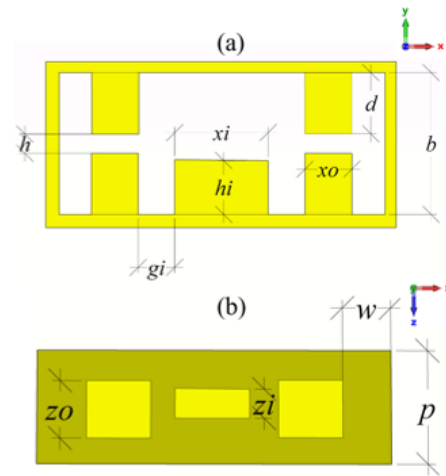


Fig. 3. HHGW-SWS. 2D Schematic front view, (a); Top view, (b). d , x_o , z_o , and p are as shown previously; $h = 0.05$ mm, $g_i = 0.42$ mm, $h_i = 0.46$ mm, $x_i = 0.6$ mm, $b = 1.27$ mm, $z_i = 0.31$ mm, $w = 0.5$ mm.

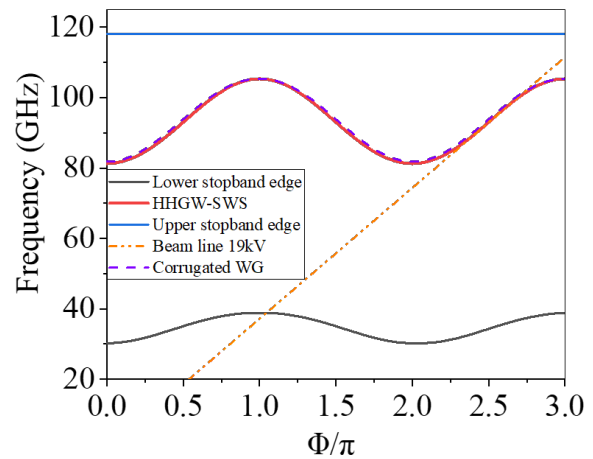


Fig. 4. Dispersion characteristic of the HHGW-SWS compared to that of the conventional corrugated WG. The upper and lower edges of the HHGW stopband are shown.

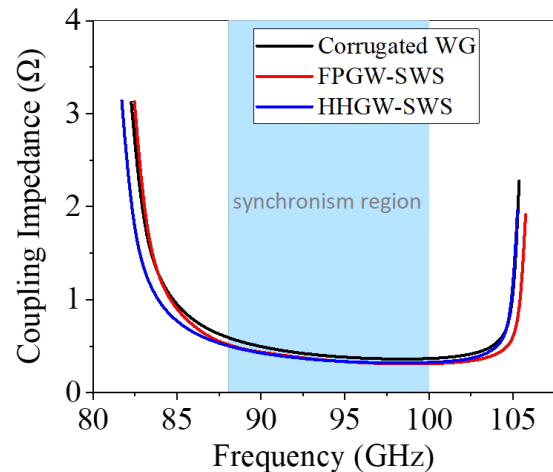


Fig. 5. Average coupling impedance for the HHGW-SWS, the full-pin GW-SWS (FPGW-SWS) and the conventional corrugated WG. The shaded area represents the estimated region of synchronism in the 86-100 GHz range.

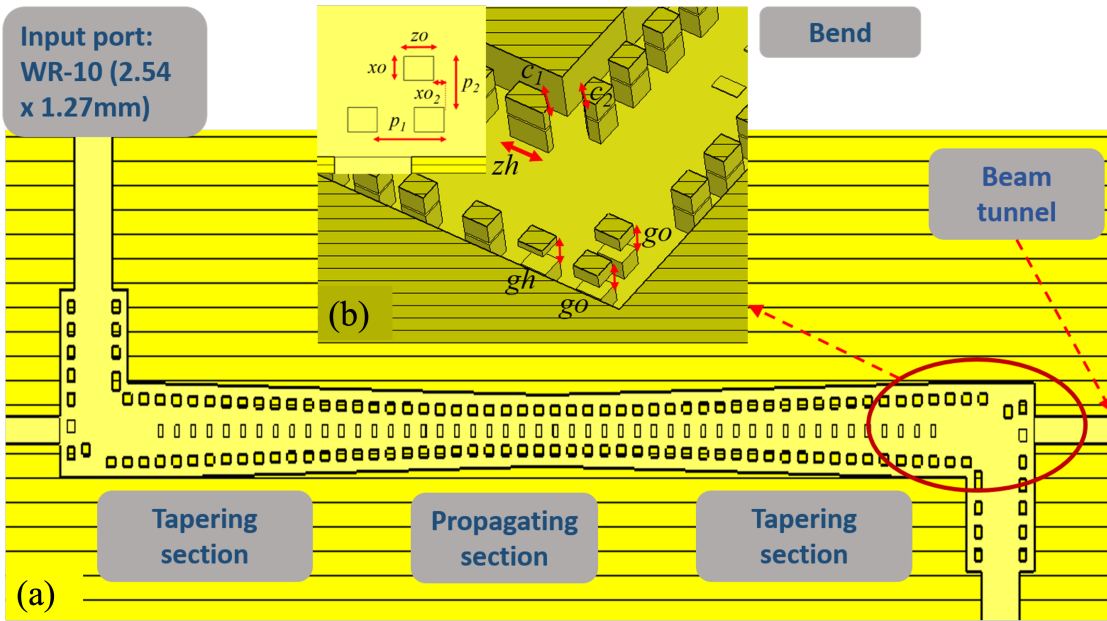


Fig. 6. Schematic of the complete HHGW-SWS (10 periods of the interaction section). (a) Bottom half top section view. (b) Close-up of coupler 90-degree bend. $xo = 0.47$ mm, $zo = 0.58$ mm, $go = 0.35$ mm, $gh = 0.51$ mm, $zh = 0.895$ mm, $p_1 = 1.3$ mm, $p_2 = 1$ mm, $xo_2 = 0.2$ mm, with chamfer on pins $c_1=0.3$ mm and $c_2=0.2$ mm.

a large effect on the lower band edge frequencies. Specifically, the larger is the air gap and the narrower is the stopband. For the design of the HHGW, the gap size of $h = 0.05$ mm is considered which leads to a total height of the waveguide of 1.27 mm, the standard WR-10 waveguide dimension. By introducing a central groove between the pins arrangement with width of 2.54 mm, the GW configuration of a WR-10 waveguide is realized as shown in Fig. 2(a). The band diagram of this waveguide is given in Fig. 2(b) where the HHGW is considered with one, two and three rows of pins repeated along the x -direction at each side of the central groove. The numerical simulations include metal lateral walls to represent the vacuum tight SWS enclosure. It can be noted from Fig.2(b) that a stopband is in all cases realized in the range 45-115 GHz and that the groove allows propagation of a single mode with same polarization and dispersion as the TE_{10} of a conventional WR-10 waveguide. Next, the SWS is designed by periodically loading the central groove with a corrugation to form the HHGW-SWS, as shown in Fig. 3. It was shown in Fig. 2(b) that the number of pin layers used at the side of the central channel does not affect the propagation mode dispersion. Thus, the case of a single layer of pins is considered throughout the paper. Additional layers can be introduced for SWS designs where the damping of higher order modes needs to be maximized. The dimensions of the optimized HHGW-SWS are given in the caption of Fig. 3.

As seen in Fig. 1, an air gap of $\sim h = 0.2$ mm for the HHGW is sufficient to generate a stopband for the upper millimeter wave band operation. However, this dimension is reduced to $h = 0.05$ mm, to minimize the reflections of the SWS input/output coupler, as shown in [14]. The dispersion characteristic of the HHGW-SWS is shown in Fig. 4, including the SWS single propagating mode dispersion and the lower/upper edges of the stopband as realized by the finite periodic structure. The Figure compares the dispersion of the SWS mode with what is obtained when the central corrugation is bounded by conventional metal walls in place of the HHGW configuration, showing no difference. The stopband from the HHGW however does not allow the higher order modes of the corrugated WG to exist. This significantly reduces potential oscillation of the TWT due to

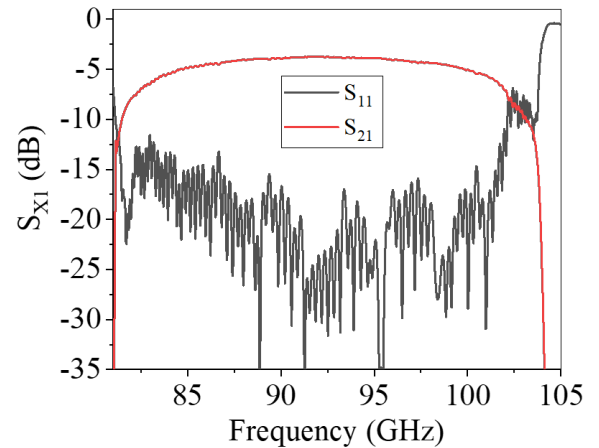


Fig. 7. S-parameters for the half-pin GW-SWS 90-period TWT simulated with a reduced copper conductivity of $\sigma = 2.89e7$ S/m.

undesired interaction with the higher order modes, a typical issue with sheet beam TWTs. Also, the beam line at 19 kV is superimposed for estimating the synchronism in the first forward spatial harmonic.

Next, the coupling impedance is calculated using the following,

$$K = \frac{|E_{zn}|^2}{2\beta_n^2 P} \quad (1)$$

where $E_{zn} = 1/p \int (E_{zn}(z) + jE_{zi}(z))e^{j(\beta_n)z} dz$, $\beta_n = \beta_0 + 2\pi n/p$, β_0 is the fundamental phase constant, n is the spatial harmonic number, β_n is the phase constant for the n^{th} space harmonic, E_z is the longitudinal electric field, p is the period of the SWS unit cell, and P is the power flow derived by the Poynting vector, [20]. A sheet beam of dimensions 1 mm x 0.2 mm, at distance of 0.08 mm above the central corrugation is considered for interaction. The average coupling impedance is calculated and compared in Fig. 5 for the three cases of the conventional corrugated SWS, the full pin

GW-SWS, and the structure proposed in this work, the HHGW-SWS, showing similar properties.

B. The HHGW-SWS coupler design

The gap waveguide technology is exploited to design a fully integrated and compact 90-degree waveguide bend to provide efficient coupling of the input/output RF signal with standard WR-10 (2.54 mm x 1.27 mm) waveguide port dimensions. The complete HHGW-SWS design consists of the interaction mode propagating section, two symmetrical tapering sections, two 90-degree waveguide bends and the beam tunnel, as shown in Fig. 6. The half-height pin arrangement that guides the signal in and out through the waveguide bends relaxes the precise machining requirements of the waveguide enclosure which becomes less critical to the coupler performance. At the same time, the pins can be arranged to block signal leakage into the beam tunnel, which is a particular convenient design feature when wide (high aspect ratio) sheet beams are used and transverse dimensions of the beam tunnel become above the cutoff. The concept was demonstrated in [8]. For the TWT here considered, the beam tunnel has dimensions 1.3 mm x 0.51 mm. Near the beam tunnel, the pins need to be locally modified to provide clearance for the beam. The position and size of the pins were optimized to allow easy fabrication and good coupling performance while allowing the beam passage. The corner pins consist of two pairs of pins with a gap of $go = 0.35$ mm and a pair of pins with a gap of $gh = 0.51$ mm. The other pin modification is $zh = 0.895$ mm. The inner corner pillars were chamfered at a 45-degree angle on the corner at 0.3 mm, and 0.2 mm respectively, to allow passage of the tooling for fabrication. The simulated scattering parameters of the complete SWS for 90 periods of the interaction section are given in Fig. 7. A reduced conductivity for the copper, $\sigma = 2.89e7$ S/m, is considered in simulation to include the effect of typical ohmic losses at this frequency range due to surface roughness achieved by machining [21]. High return loss, more than 15 dB, is shown in the 87-101 GHz range. The tapering section gradually converts the TE₁₀ mode from the WR-10 port to the hybrid mode of the interaction section across 20 periods on each side.

C. Particle-in-cell simulations

The interaction between electron beam and RF signal is analyzed numerically via the particle-in-cell solver of CST Particle Studio. A total of 90 periods of the HHGW-SWS are simulated in a single section TWT. After numerical optimization, the beam voltage is set at 21 kV with a current of 0.3 A. The beam widest dimension is set at 1 mm while the narrow dimension is 0.2 mm. The cross section of the simulated sheet beam has rounded edges of radius $r = 0.1$ mm. An uniform magnetic field of 0.9 T is used in simulation to focus the electron beam. The small signal gain and output power curves in the frequency range of interest are shown in Fig. 8(a). As can be noted, a 10-GHz instantaneous 3-dB bandwidth in the 89-99 GHz frequency range with a minimum power gain of 25 dB is realized. In Fig. 8(b), the frequency spectrum of the output and input signal at 90 GHz, where potential for low band edge oscillations is higher, can be seen for a simulation running time of 15 ns, showing high spectral purity and no sign of oscillation. The input-output power characteristic simulated at the frequency of 93.5 GHz is shown in Fig. 9, indicating a saturated value of output power around 160 W. In the conditions of maximum power generation, the E -field distribution along the HHGW-SWS is analyzed to confirm that no enhancement of the field is realized within the pins gap that could pose a breakdown concern. Similarly, surface current for the HHGW-SWS is found to

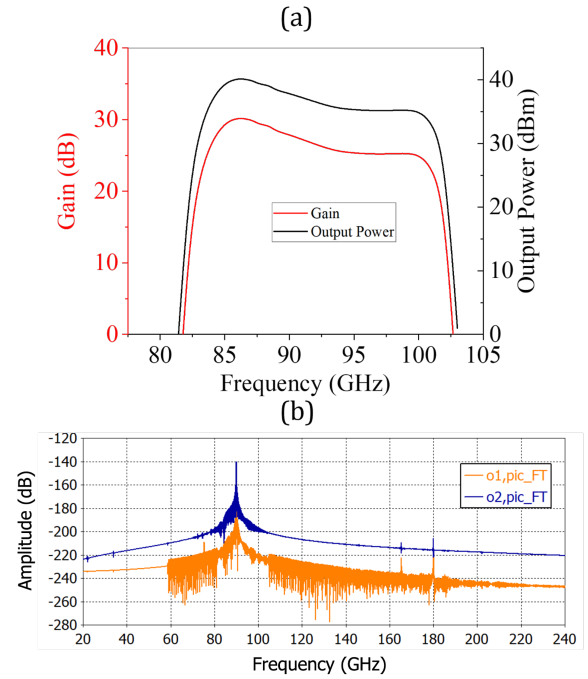


Fig. 8. (a) Frequency vs Gain, and Frequency vs Output power for the half-pin GW-SWS. (b) Fast Fourier transform of the output and input signal at 90 GHz obtained when running the simulation for 15 ns (in blue and orange, respectively).

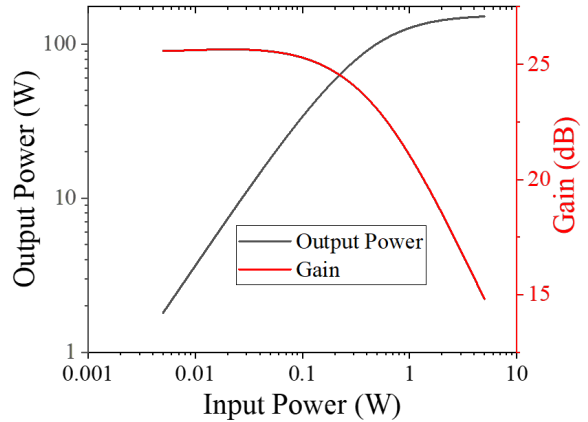


Fig. 9. Input power vs Output power, and Input power vs Gain for the half-pin GW-SWS.

be of the same level as in the counterpart corrugated waveguide which suggests comparable RF heating. To verify stability of the tube, the gain-stability equation for a single section TWT is used, as given in Equation (2), where G represents the gain and S_{xx} are the S-parameters of the SWS in dB units [22]. From the cold characteristics simulated it can be calculated from (2) that the designed TWT is stable up to a gain of ~ 35 dB.

$$G - |S_{11}| - |S_{22}| - |S_{21}| < 0 \quad (2)$$

III. COLD TEST MEASUREMENTS

A prototype of the complete HHGW-SWS was realized in aluminium to ease the machining for an interaction section of 10 periods as shown in Fig. 10. The piece was fabricated in two halves via

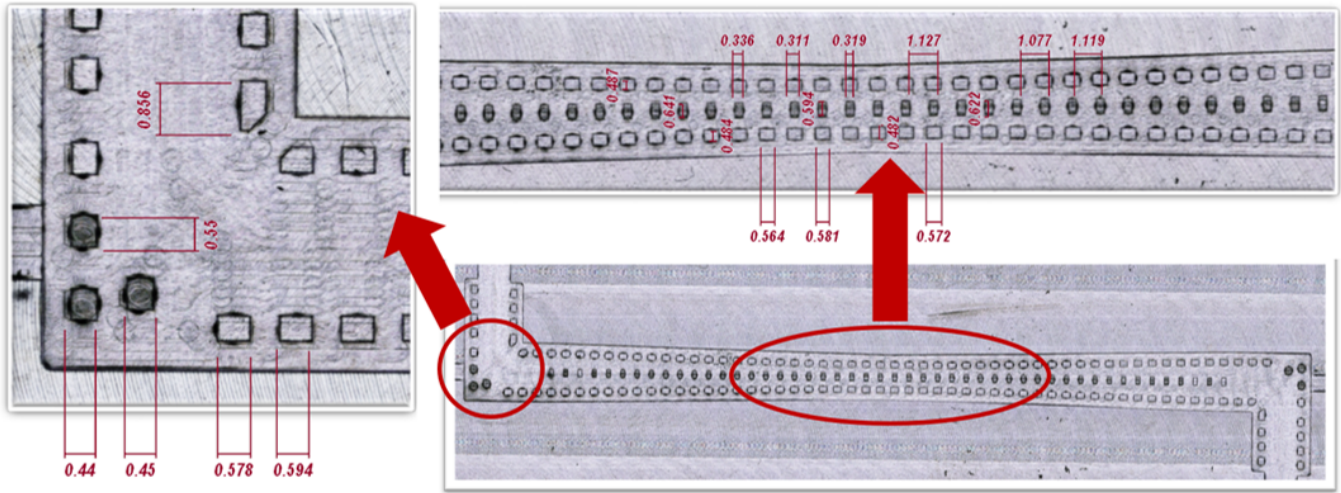


Fig. 10. Microscopic view of the bottom half of the fabricated GW-SWS, zooming into the bend and propagation section. Dimension values are in mm.

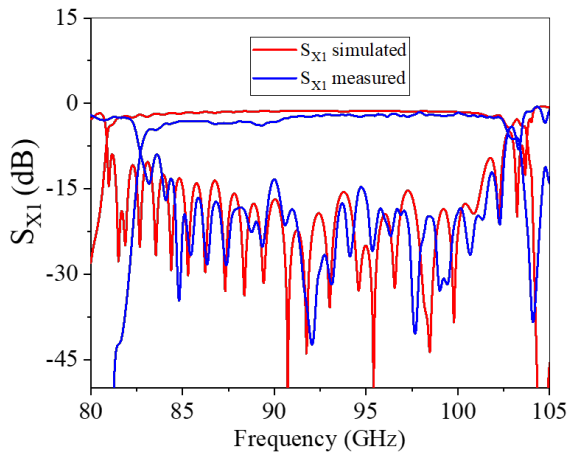


Fig. 11. S-parameters of the aluminium 10-period prototype for the half-pin GW-SWS, simulated vs measured.

CNC machining, at a tooling speed of 50000 RPM air turbine using a 0.4 mm tooling piece. Inspection of the parts using the Olympus LEXT laser confocal microscope shows dimensional accuracy $\sim \pm 20 \mu\text{m}$. The measured S -parameters are compared with simulated results in Fig. 11. A reduced conductivity of $\sigma = 1.78e7 \text{ S/m}$ is used in simulation for aluminium. The good agreement between the S_{11} measured and simulated can be noted, with a maximum value of -15 dB. The achieved surface roughness R_a was measured at approximately 200 nm which informed the correspondent reduced conductivity to be used in simulation as per the empirical formula in [23], [24].

IV. SENSITIVITY ANALYSIS

Misalignment of the two fabricated SWS halves is a common issue of TWT assembly and one that can be critical for SWS performance, for example in folded waveguides a misalignment of $10 \mu\text{m}$ can cause severe alterations to the designed dispersion characteristics [5]. It is important to note that the proposed HHGW-SWS is not sensitive to misalignment defects in fabrication and thus, from this viewpoint they are as robust as the configurations with pins only at the bottom plate, such as the full pin GW-SWS or the structure proposed in [8]. As shown in Fig. 12(a)-(b), a misalignment as large

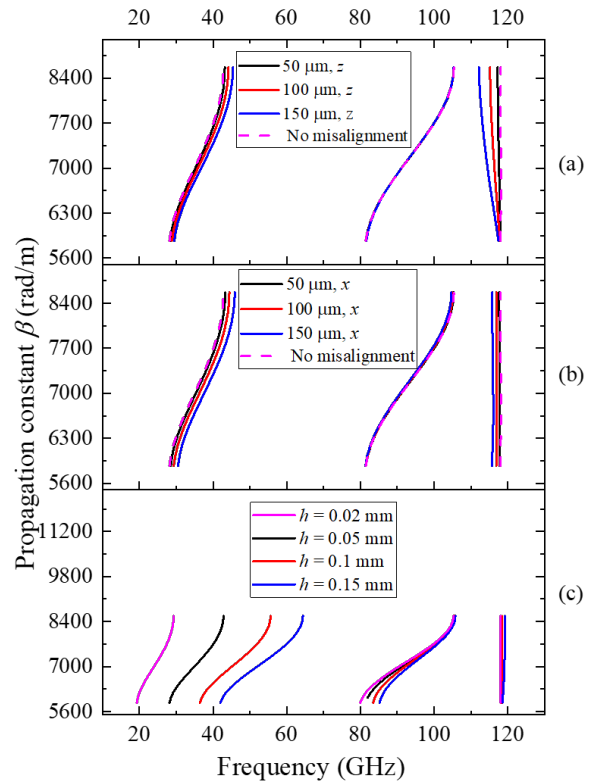


Fig. 12. Dispersion characteristics for HHGW-SWS with a misalignment of 50 μm , 100 μm and 150 μm , in (a) z and (b) x direction, compared to no misalignment (dashed line); (c) Sensitivity study on the dispersion characteristic when varying h .

as 150 μm in both the x and z direction does not have a significant effect on the interaction mode dispersion characteristic. In contrast, Fig. 12(c) shows increased sensitivity to the air gap dimension, h . It can be seen that a larger gap size shifts the cutoff frequency of the mode, which can potentially reduce the TWT bandwidth. Precision machining however typically ensures dimensional accuracy well below the simulated minimum variation of $\pm 50 \mu\text{m}$.

V. CONCLUSION

In this paper, we have introduced the use of the Half-Height pin-based gap waveguide to assist the design of SWSs in the upper millimeter wave frequency range. The concept was demonstrated numerically for the design of a single section broadband TWT operating in the 89-99 GHz range with a minimum gain of 25 dB. A prototype of the complete HHGW-SWS design was realized via CNC machining and measured with a good agreement of reflections around -15 dB in the operating bandwidth and transmission loss of approximately 2 dB compared to simulations. The HHGW-SWS retains all the properties previously demonstrated for electromagnetic bandgap waveguide-assisted SWSs including flexible design of the input/output coupler, easy design of the beam tunnel for dimensions above the cutoff, and integration of filtering functionalities. However, compared to the classical pin-based periodic structures for SWS design proposed in the literature, the HHGW features have significantly lower aspect ratio and/or reduced vertical dimension making them easier to realize via both micro-machining and UV-LIGA. We demonstrated that the structure is robust to misalignment issues in assembly, and that required tolerances for the air gap dimension are compatible with typical fabrication techniques utilized at these frequencies and above. It is important to note that a configuration of HHGW-SWS utilizing a single row of pins at the sides of the central corrugation was chosen to minimize complexity of geometry. However, the number of rows can be increased for SWS designs where the damping of unwanted modes within the HH-pin structures is critical to correct operation. This topology can be successfully applied to alternative conventional SWS geometries based on a rectangular waveguide enclosure and can be successfully scaled to higher frequency ranges.

ACKNOWLEDGMENTS

The Authors would like to acknowledge the use of the High End Computing facility at Lancaster University for the expedition of the PIC simulations.

REFERENCES

- [1] H. Cheng, X. Zhu, F. Hou, W. Wang, L. Shen and S. Hu, "Compact 31-W 96-GHz Amplifier Module in GaN-MEMS for Wireless Communications," in *IEEE Transactions on Microwave Theory and Techniques*, vol. 70, no. 2, pp. 1233-1241, Feb. 2022, doi: 10.1109/TMTT.2021.3121003.
- [2] Claudio Paoloni, Diana Gamzina, Rosa Letizia, Yuan Zheng and Neville C. Luhmann Jr. (2021) "Millimeter wave traveling wave tubes for the 21st Century", in *Journal of Electromagnetic Waves and Applications*, 35:5, 567-603, DOI: 10.1080/09205071.2020.1848643.
- [3] A. M. Cook, E. L. Wright, K. T. Nguyen, C. D. Joye, J. C. Rodgers, R. L. Jaynes, I. A. Chernyavskiy, F. N. Wood, B. S. Albright, D. K. Abe, J. P. Calame, B. Levush, D. E. Pershing, J. Atkinson, and T. Kimura, "Demonstration of a W-Band Traveling-Wave Tube Power Amplifier With 10-GHz Bandwidth," in *IEEE Transactions on Electron Devices*, vol. 68, no. 5, pp. 2492-2498, May 2021, doi: 10.1109/LED.2021.3068926.
- [4] J. Chen, Z. Wang, F. Wang, C. Gao, J. Li, Q. Xie, Z. Zi, J. Cai, J. Feng, "Demonstration of a Broadband W-Band Microwave Power Module With Improved Gain Flatness," in *IEEE Electron Device Letters*, vol. 43, no. 8, pp. 1335-1338, Aug. 2022, doi: 10.1109/LED.2022.3185157.
- [5] R. L. Ives, "Microfabrication of high-frequency vacuum electron devices," in *IEEE Transactions on Plasma Science*, vol. 32, no. 3, pp. 1277-1291, June 2004, doi: 10.1109/TPS.2004.827595.
- [6] M. Mineo and C. Paoloni, "Double-Corrugated Rectangular Waveguide Slow-Wave Structure for Terahertz Vacuum Devices," in *IEEE Transactions on Electron Devices*, vol. 57, no. 11, pp. 3169-3175, Nov. 2010, doi: 10.1109/TED.2010.2071876.
- [7] L. R. Billa, M. N. Akram, C. Paoloni and X. Chen, "H-E Plane Loaded Slow Wave Structure for W-Band TWT," in *IEEE Transactions on Electron Devices*, vol. 67, no. 1, pp. 309-313, Jan. 2020, doi: 10.1109/TED.2019.2955825.
- [8] R. Letizia, M. Mineo and C. Paoloni, "Photonic Crystal-Structures for THz Vacuum Electron Devices," in *IEEE Transactions on Electron Devices*, vol. 62, no. 1, pp. 178-183, Jan. 2015, doi: 10.1109/TED.2014.2366639.
- [9] N. Shi, H. Wang, D. Xu, Z. Wang, Z. Lu, H. Gong, D. Liu, Z. Duan, Y. Wei, Y. Gong, "Study of 220 GHz Dual-Beam Overmoded Photonic Crystal-Loaded Folded Waveguide TWT," in *IEEE Transactions on Plasma Science*, vol. 47, no. 6, pp. 2971-2978, June 2019, doi: 10.1109/TPS.2019.2914164.
- [10] E. Tahanian and G. Dadashzadeh, "A novel gap-groove folded-waveguide slow-wave structure for G-band traveling-wave tube," in *IEEE Transactions on Electron Devices*, vol. 63, no. 7, pp. 2912-2918, July 2016, doi: 10.1109/TED.2016.2564740.
- [11] Y. Wan, J. Wang, X. Li, Q. Liu, G. Shu, W. Jiang, Z. Wu, and Y. Luo, "Design, Microfabrication, and Experiment of a Compact Mode Selection Filter for Sub-Terahertz Sheet Beam Traveling-Wave Tubes," in *IEEE Transactions on Microwave Theory and Techniques*, vol. 70, no. 8, pp. 3870-3876, Aug. 2022, doi: 10.1109/TMTT.2022.3186209.
- [12] H. S. Sudhamani, J. Balakrishnan and S. U. M. Reddy, "Investigation of Instabilities in a Folded-Waveguide Sheet-Beam TWT," in *IEEE Transactions on Electron Devices*, vol. 64, no. 10, pp. 4266-4271, Oct. 2017, doi: 10.1109/TED.2017.2736065.
- [13] Kildal, Per-Simon and Alfonso, E. and Valero-Nogueira, A. and Rajo-Iglesias, Eva, "Local Metamaterial-Based Waveguides in Gaps Between Parallel Metal Plates" in *IEEE Antennas and Wireless Propagation Letters*, vol. 8, pp. 84-87, 2009, doi:10.1109/LAWP.2008.2011147.
- [14] A. Z. Abozied and R. Letizia, "Investigation of gap waveguide-based slow wave structure for millimeter wave travelling wave tubes," 2021 14th UK-Europe-China Workshop on Millimetre-Waves and Terahertz Technologies (UCMMT), 2021, pp. 1-3, doi: 10.1109/UCMMT53364.2021.9569878.
- [15] A. Z. Abozied and R. Letizia, "Gap waveguides for millimeter wave slow wave structures," 2021 22nd International Vacuum Electronics Conference (IVEC), 2021, Rotterdam, Netherlands, pp. 1-2, doi: 10.1109/IVEC51707.2021.9722439.
- [16] A. Z. Abozied and R. Letizia, "Parametric Study of Pin-based Gap Waveguide for Millimeter Wave Slow Wave Structures," 2022 15th UK-Europe-China Workshop on Millimetre-Waves and Terahertz Technologies (UCMMT), 2022, Tønsberg, Norway, pp. 1-3, doi: 10.1109/UCMMT56896.2022.9994829.
- [17] F. Fan, J. Yang and P. -S. Kildal, "Half-height pins - a new pin form in gap waveguide for easy manufacturing," 2016 10th European Conference on Antennas and Propagation (EuCAP), Davos, Switzerland, 2016, pp. 1-4, doi: 10.1109/EuCAP.2016.7481931.
- [18] F. Fan, J. Yang, V. Vassilev and A. U. Zaman, "Bandwidth Investigation on Half-Height Pin in Ridge Gap Waveguide," in *IEEE Transactions on Microwave Theory and Techniques*, vol. 66, no. 1, pp. 100-108, Jan. 2018, doi: 10.1109/TMTT.2017.2732983.
- [19] CST Studio Suite, [online] Available: <https://www.3ds.com/products-services/simulia/products/cst-studio-suite/>.
- [20] R. Carter, "Microwave and RF vacuum electronic power", Cambridge University Press, 2018.
- [21] D. Gamzina et al., "Nanoscale Surface Roughness Effects on THz Vacuum Electron Device Performance," in *IEEE Transactions on Nanotechnology*, vol. 15, no. 1, pp. 85-93, Jan. 2016, doi: 10.1109/TNANO.2015.2503984.
- [22] A. S. Gilmour, "Principles of Travelling wave Tubes", 1994.
- [23] B. B. Yang, M. P. Kirley and J. H. Booske, "Theoretical and Empirical Evaluation of Surface Roughness Effects on Conductivity in the Terahertz Regime," in *IEEE Transactions on Terahertz Science and Technology*, vol. 4, no. 3, pp. 368-375, May 2014, doi: 10.1109/TTHZ.2014.2310121.
- [24] M. V. Lukic and D. S. Filipovic, "Modeling of 3-D Surface Roughness Effects With Application to μ -Coaxial Lines," in *IEEE Transactions on Microwave Theory and Techniques*, vol. 55, no. 3, pp. 518-525, March 2007, doi: 10.1109/TMTT.2007.891688.